REVIEW

Non-conventional Strain Glasses

Wenjia Wang[1] · Yuanchao Ji[1] · Minxia Fang[1] · Xiaobing Ren[1,2]

Abstract Strain glass, a short-range strain-ordered state of martensitic/ferroelastic material, has drawn much interest in recent years due to its novel properties unattainable in martensitic materials. So far, typical or conventional strain glasses have been reported to be characterized by nano-sized martensitic domains formed from a homogeneous parent phase matrix. This article reviews the recent progress in "non-conventional strain glass," which is different from the conventional strain glasses reported so far. We first introduce a "reentrant strain glass," where strain glass nanodomains are formed from a martensitic phase instead of from a parent phase. The reentrant strain glass can show low modulus and high damping properties over a wide temperature range. The second non-conventional strain glass is a "spinodal strain glass" produced by a spinodal decomposition in its early stage. This unique strain glass is formed from a nanoscale compositionally inhomogeneous parent phase (by spinodal decomposition). The spinodal strain glass demonstrates high-damping Elinvar effect over an ultrawide temperature range. These non-conventional strain glass alloys may have potential for novel applications as new structural–functional materials.

Keywords Strain glass · Reentrant glass transition · Spinodal decomposition · High damping · Elinvar

✉ Yuanchao Ji
  jyc.xjtu@xjtu.edu.cn

✉ Xiaobing Ren
  REN.Xiaobing@nims.go.jp

1 Frontier Institute of Science and Technology, State Key Laboratory for Mechanical Behavior of Materials and MOE Key Laboratory for Nonequilibrium Synthesis and Modulation of Condensed Matter, Xi'an Jiaotong University, Xi'an 710049, China

2 Center for Functional Materials, National Institute for Materials Science, Tsukuba, Ibaraki 305-0047, Japan

Introduction

Strain glass (STG), the conjugate glassy state of martensitic/ferroelastic phase, has been reported in many martensitic/ferroelastic alloys and ceramics, including Ni-rich Ti–Ni, TiNi-based, TiPd-based, β-Ti-based, Mg-based and magnetic shape memory alloys, ceramics, and ferroelectric materials [1–15]. They are characterized by the existence of nano-sized martensitic domains over a broad temperature range [1–15]. The response of strain glass under stimuli can involve only a growth process *without* nucleation due to nanodomains acting as the nuclei. Due to these nanodomains, the strain glass possesses many interesting and technologically important properties of strain glass, e.g., superelasticity with slim hysteresis, low field-triggered large magnetostriction, Invar (negligible change in thermal expansion with temperature changes) effect, and Elinvar (negligible change in elastic modulus with temperature changes) effect over a wide temperature range [2–4, 16, 17].

Strain glass is formed by the atomic/nanoscale randomness which disrupts the formation of normal martensite [1–4, 18–20]. By doping defects into a martensitically unstable alloy, the atomic/nanoscale randomness is introduced, leading to the disappearance of long-range strain

ordering; instead, the alloy undergoes a strain glass transition into *nano-sized martensitic domains embedded in the homogeneous parent phase matrix*, with long-range strain disordering but short-range strain ordering [1–4]. As a consequence, the average structure of strain glass usually shows the structure of the parent phase, which is usually cubic, e.g., B2 structure for Ni-rich Ti–Ni and TiNi-based strain glass alloys [1–4]. Contrasting with the above-mentioned typical or "conventional" strain glass, two "nonconventional" strain glasses have been reported recently [21, 22] and interesting properties have been revealed. In the following, we shall briefly review these new findings and will make an outlook for the potential of these nonconventional strain glasses as novel types of functional/structural materials.

Reentrant Strain Glass

Contrast with the conventional strain glass which is formed from a high-temperature strain-disordered state (parent phase) into a low-temperature strain glass state (characterized by nano-sized martensite domains), a special type of strain glass (called reentrant strain glass) has been found to exist, which is characterized by the formation of nanosized martensitic domains (with symmetry A) from a macroscopic martensite of a different structure (with symmetry B). This unusual type of strain glass is named "reentrant strain glass" (RSTG) [21], because it seems that a long-range strain-ordered system (normal martensite) reenters into a frozen disordered glassy state. The reentrant strain glass transition is physically parallel to reentrant spin glass transition and reentrant relaxor transition in ferromagnetic and ferroelectric systems [23, 24]. In the following, we shall show the macroscopic and microscopic features of reentrant strain glass and their unique properties, as well as the origin of this non-conventional strain glass.

Macroscopic Characterization of Reentrant Strain Glass Transition

As shown in Fig. 1, $Ti_{50}Ni_{34}Cu_{16}$ shape memory alloy undergoes the RSTG transition from the B19 martensite to the reentrant strain glass below B2–B19 martensitic transformation. Upon cooling, $Ti_{50}Ni_{34}Cu_{16}$ firstly transforms from B2 parent phase into B19 martensite at T_{B19} ~ 330 K, characterized by a structural change from cubic to orthorhombic (Fig. 1a), a sharp peak in heat flow curve (Fig. 1b), thermal hysteresis of electrical resistivity (Fig. 1c), and a large drop of modulus and a sharp peak of internal friction (tan δ) (Fig. 1d).

The reentrant strain glass transition occurs at T_{rg} ~ 220 K, supported by five macroscopic evidences. (I) The XRD results in Fig. 1a indicate that the average structure does not change from 293 to 133 K. (II) No exothermal peak exits in the DSC cooling curve of Fig. 1b but a turning point shows up at T_{rg}, as shown in the derivative of heat flow curve (inset of Fig. 1b). (III) Electrical resistivity curves show a slope change at T_{rg} but no thermal hysteresis (Fig. 1c). (IV) During the cooling process, the modulus starts to increase at T_{rg} and in the same time the internal friction shows a peak at T_{rg} (Fig. 1d). What's more, both the storage modulus and internal friction curves display frequency dispersion around T_{rg}. The frequency-dependent peak temperature of internal friction obeys the Vogel–Fulcher relation. (V) Ergodicity is broken as shown in the field-cooling/zero-field-cooling (FC/ZFC) curves (Fig. 1e). These five features are consistent with those of previous strain glass transitions [1–4]. Therefore, $Ti_{50}Ni_{34}Cu_{16}$ undergoes firstly B2–B19 martensitic transition at T_{B19} and then reentrant strain glass transition at T_{rg}.

Here, the interesting point is that the average structure of reentrant strain glass belongs to the B19 orthorhombic phase instead of the B2 parent phase and keeps invariant during the RSTG transition. Note that the position of the characteristic B19 peaks $(002)_o$, $(020)_o/(111)_o$, and $(012)_o$ show a weak shift upon cooling, whereas the width of these peaks shows clear broadening from 293 to 133 K as shown in a quantitative analysis of broadening in Fig. 2, which is due to the appearance and growth of nanodomains similar to the conventional strain glass transition [12].

Microscopic Characterization of Reentrant Strain Glass

Figure 3 shows the microscopic picture of reentrant strain glass in $Ti_{50}Ni_{34}Cu_{16}$ shape memory alloy. At 293 K, the morphology of $Ti_{50}Ni_{34}Cu_{16}$ alloy shows typical martensitic plates and the corresponding diffraction pattern shows the typical 1/2 diffraction spots caused by the shuffle displacement of B19 structure [25, 26]. When cooling to 133 K, the martensitic domains show nearly no change, while additional 1/4 diffraction spots appear in the diffraction pattern.

By comparing the high-resolution TEM images at 293 K and 133 K, it can be clearly seen that when cooling from 293 to 133 K during the reentrant strain glass transition, some nano-sized domains appear, embedded in the large B19 martensitic domain as shown in Fig. 3b. Furthermore, the modulation period of these nanodomains is 4, being consistent with the additional 1/4 diffraction spots, suggesting the local symmetry of these nanodomains is 4H [21, 27]. In short, during the reentrant strain glass
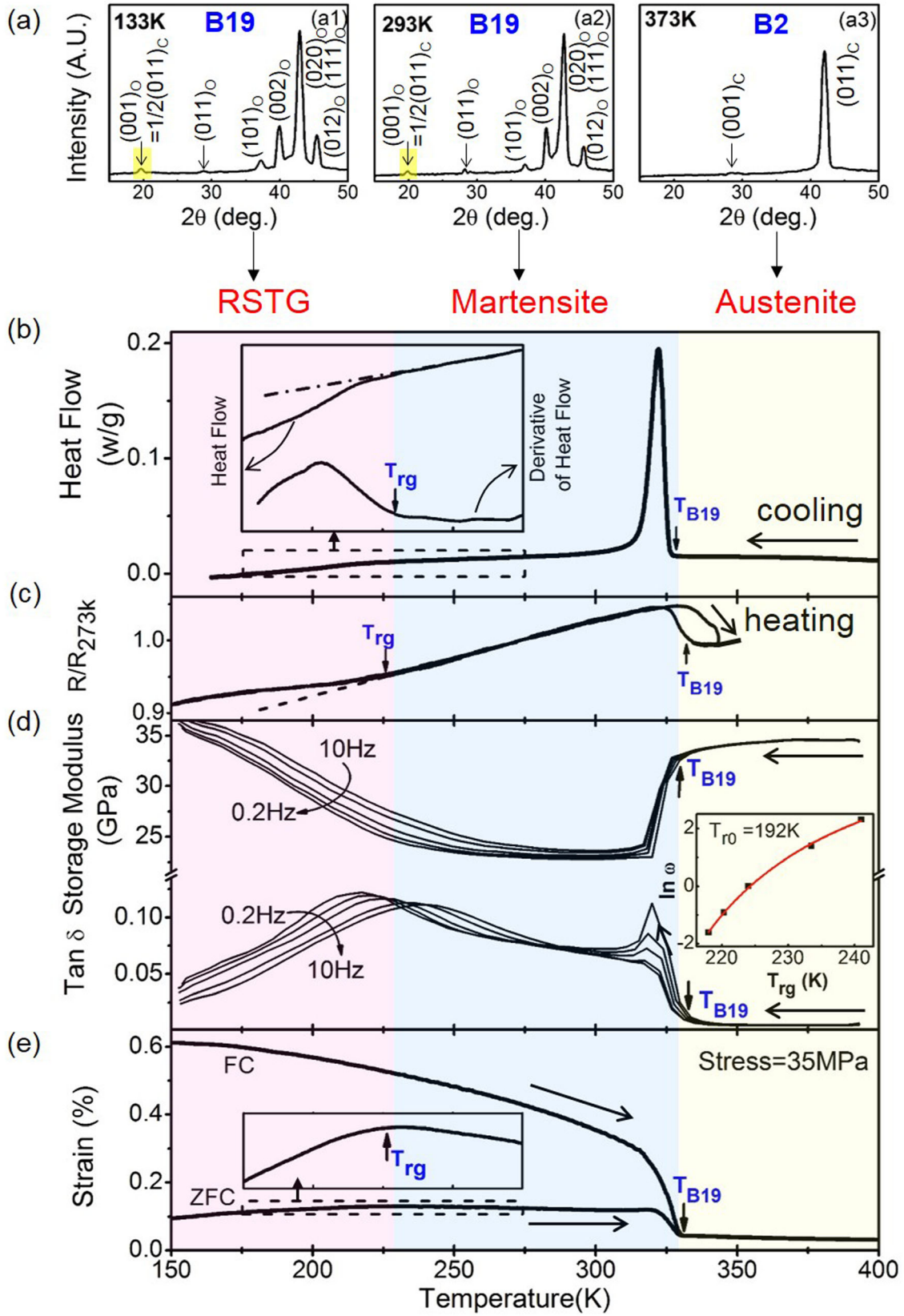
Fig. 2 In situ X-ray diffraction patterns of $Ti_{50}Ni_{34}Cu_{16}$ alloy upon cooling from 293 to 133 K. Note that the width of $(002)_o$, $(020)_o$/$(111)_o$, and $(012)_o$ peaks, characterized by the full width at half maximum ($W_{1/2}$), becomes broader upon cooling [21]. Reprinted from *Acta Materialia,* Vol 226, Wenjia Wang, Yuanchao Ji, Minxia Fang, Dong Wang, Shuai Ren, Kazuhiro Otsuka, Yunzhi Wang, Xiaobing Ren, Reentrant strain glass transition in Ti–Ni–Cu shape memory alloy, Page 117, 618, Copyright 2022, with permission from Elsevier
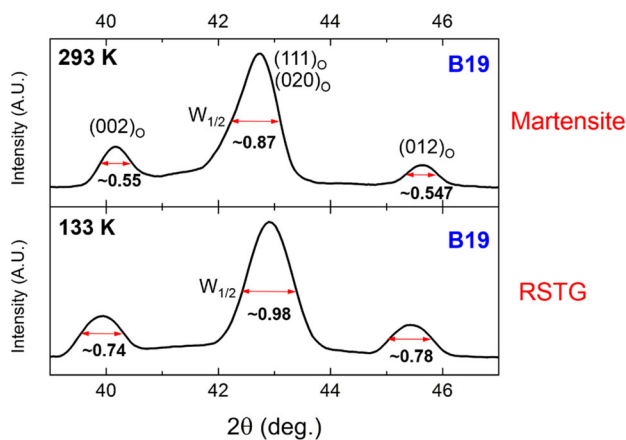
transition, the nanodomains of 4H symmetry emerge within the large B19 martensitic plates.

Distinctiveness of Reentrant Strain Glass

The new $Ti_{50}Ni_{50-x}Cu_x$ phase diagram including the reentrant strain glass region is presented in Fig. 4a. When $x < 7.5$, B2–B19' martensitic transition occurs; when $7.5 \leq x \leq 15$, B2–B19–B19' martensitic transition occurs; when $x > 15$, the system firstly undergoes B2–B19 martensitic transition and then the reentrant strain glass transition from B19 martensite to the 4H strain glass.

The reentrant strain glass transition shares many glassy features with the conventional strain glass transition, such as no latent heat and no hysteresis during the glass transition, no macroscopic symmetry (average structure)

change through the glass transition, the existence of frequency dispersion in storage modulus and internal friction curves, breaking the ergodicity in ZFC/FC curves, and the emergence of short-range strain-ordered nanodomains.

Nevertheless, fundamental differences exist between the reentrant strain glass and conventional strain glass. As shown in Figs. 1, 3, and 4, the reentrant strain glass transition is from the strain-ordered martensite to the glassy state, whereas the conventional strain glass transition is from the strain-disordered austenite to the glassy state. Therefore, the macroscopic symmetry and microstructure of two glasses are different: the former has the temperature-invariant martensitic symmetry in XRD data (e.g., B19 structure in $Ti_{50}Ni_{50-x}Cu_x$) and the large martensitic domains/plates as the matrix in microstructural observations [21]; the latter has the temperature-invariant austenitic symmetry in XRD data (e.g., B2 structure in $Ti_{50-x}Ni_{50+x}$) and no large martensitic domains in microstructural observations [1–4, 28].

Furthermore, since the reentrant strain glass transition produces the unusual microstructure of low-symmetry martensitic nanodomains embedded in the large high-symmetry martensitic matrix instead of in the austenitic matrix, unique properties such as ultra-low modulus and high damping property over a large temperature window have been found, as shown in Fig. 5 [21].

Understanding of Reentrant Strain Glass Formation

Figure 6 provides schematic and qualitative understandings of the emergence of reentrant strain glass transition. In the $Ti_{50}Ni_{50-x}Cu_x$ system, Cu dopants act as the point defects and can change the transition temperature (a global effect) and produce local lattice distortions (a local effect) [18]. Cu dopants produce an increased thermodynamic stability of B19 phase relative to B2 and B19' phases, i.e., Cu dopants stabilize B19 phase instead of B2 phase or B19' phase, as evidenced by an increase of T_{B19} with increasing Cu concentration and a decrease of $T_{B19'}$ with increasing Cu concentration. In short, Cu dopants favor the 1st-step B2–B19 martensitic transformation but prevent the 2nd-step B19–B19' transition.

Whether B19 phase can transform into the B19' phase depends on the Cu concentration. With increasing the Cu concentration, both global and local effects from Cu dopants will become stronger: the driving force for B19–B19' transition decreases as characterized by the $T_{B19'}$ decrease (global effect); the local energy barriers caused by the point defects will be increased, favoring the formation of nanodomains but impeding the formation of long-range ordered martensitic phase (local effect). As a result, when the Cu dopant concentration x is high enough, the driving force of B19–B19' transition will become much smaller
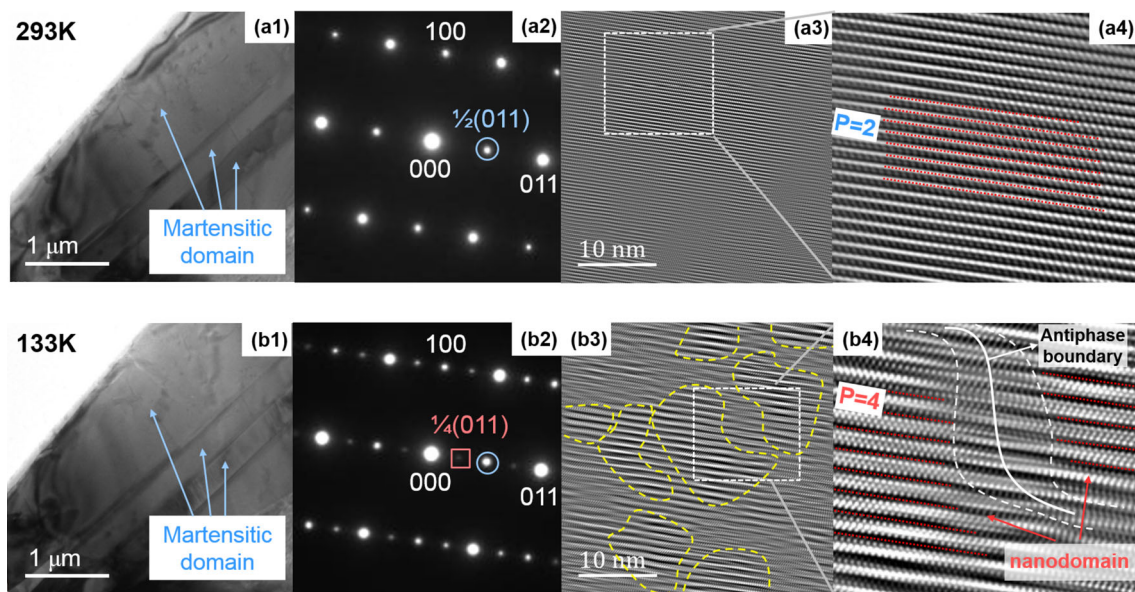
Fig. 3 Microscopic characterization of reentrant strain glass of Ti$_{50}$Ni$_{34}$Cu$_{16}$. **a** 293 K (below T_{B19} but above T_{rg}). **b** 133 K (below T_{rg}). Long-range ordered martensitic domains show nearly no difference during reentrant strain glass transition upon cooling, but additional 1/4 diffraction spots show up at 133 K in the diffraction pattern of (b2). (a3) and (b3) show HREM image within the martensitic domains in (a1) and (b1), respectively. Short-range strain-ordered nanodomains appear within the large martensitic plate below T_{rg} in (b3). (a4) and (b4), the enlarged image from the squared area in (a3) and (b3), respectively, shows that the modulation period of the nanodomains in (b4) is 4 instead of 2 of B19 crystal structure in (a4). [21] Reprinted from *Acta Materialia,* Vol 226, Wenjia Wang, Yuanchao Ji, Minxia Fang, Dong Wang, Shuai Ren, Kazuhiro Otsuka, Yunzhi Wang, Xiaobing Ren, Reentrant strain glass transition in Ti–Ni–Cu shape memory alloy, Page 117, 618, Copyright 2022, with permission from Elsevier
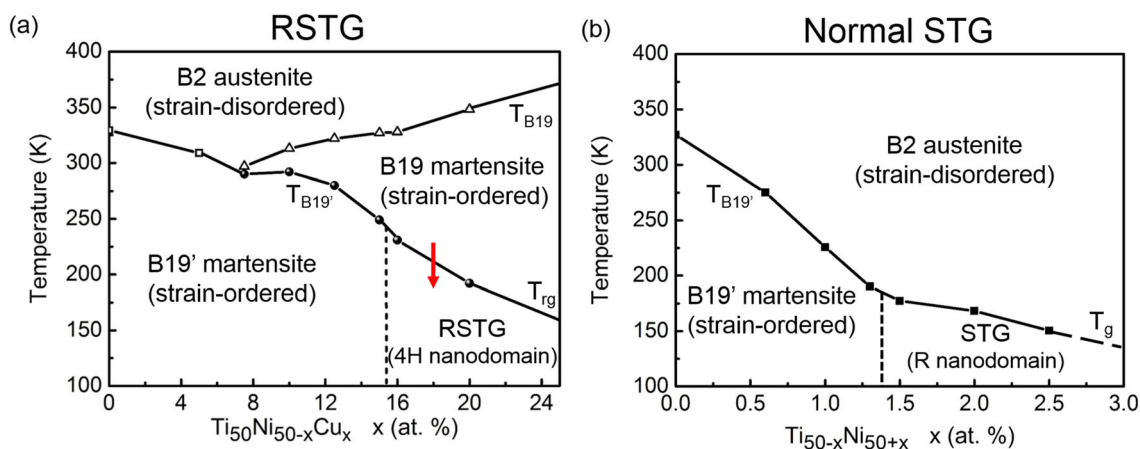

Fig. 4 a Reentrant strain glass phase diagram of Ti$_{50}$Ni$_{50-x}$Cu$_x$, where B2 austenite, B19 martensite and B19' martensite, and RSTG with local 4H symmetry represent the strain-disordered, two strain-ordered, and glassy phases, respectively. **b** Conventional strain glass phase diagram of Ti$_{50-x}$Ni$_{50+x}$, where B2 austenite, B19' martensite, and STG with local R symmetry represent the strain-disordered, strain-ordered, and glassy phases, respectively. [21] Reprinted from *Acta Materialia,* Vol 226, Wenjia Wang, Yuanchao Ji, Minxia Fang, Dong Wang, Shuai Ren, Kazuhiro Otsuka, Yunzhi Wang, Xiaobing Ren, Reentrant strain glass transition in Ti–Ni–Cu shape memory alloy, Page 117, 618, Copyright 2022, with permission from Elsevier

and lose the competitiveness against the increased local energy barriers, thereby the B19–B19' transition disappears and the reentrant strain glass appears instead.

For the reentrant strain glass transition, the B19' phase cannot be reached as described above. However, the system can locally transform into other states that are between

B19 phase and B19' phase. This actually has happened in the Ni-rich Ti–Ni strain glass in Fig. 4b: the B2–B19' martensitic transition is suppressed and yet the system goes into the strain glass with local R symmetry, where the R phase is an intermediate phase between B2 phase and B19' phase. Similarly, in the Ti$_{50}$Ni$_{34}$Cu$_{16}$, the system locally

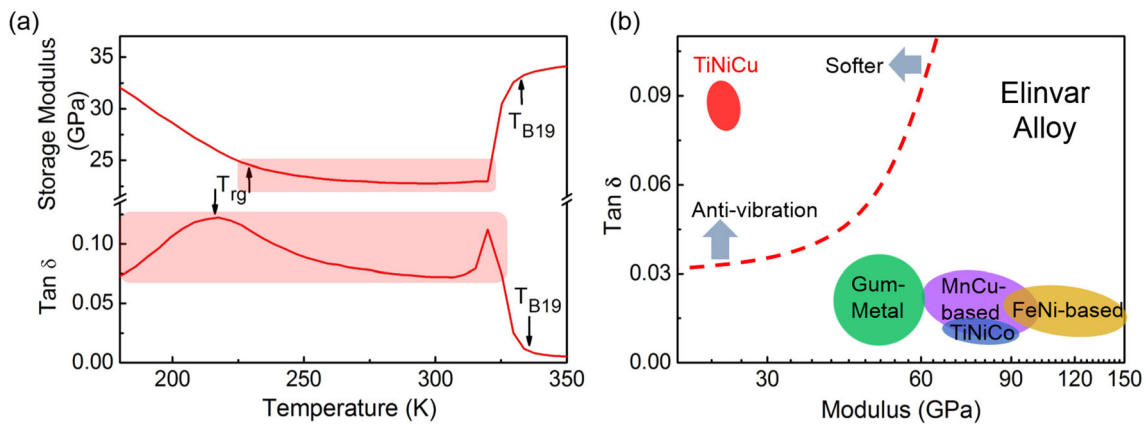**Fig. 5 a** Ultra-low modulus and high damping property in reentrant strain glass of $Ti_{50}Ni_{34}Cu_{16}$. Storage modulus keeps constant around 24 GPa from 225 to 325 K, and tan δ maintains above 0.075 from 180 to 325 K. **b** Comparison of modulus vs. damping (tan δ) of different Elinvar alloys. [21] Reprinted from *Acta Materialia,* Vol 226, Wenjia Wang, Yuanchao Ji, Minxia Fang, Dong Wang, Shuai Ren, Kazuhiro Otsuka, Yunzhi Wang, Xiaobing Ren, Reentrant strain glass transition in Ti–Ni–Cu shape memory alloy, Page 117, 618, Copyright 2022, with permission from Elsevier
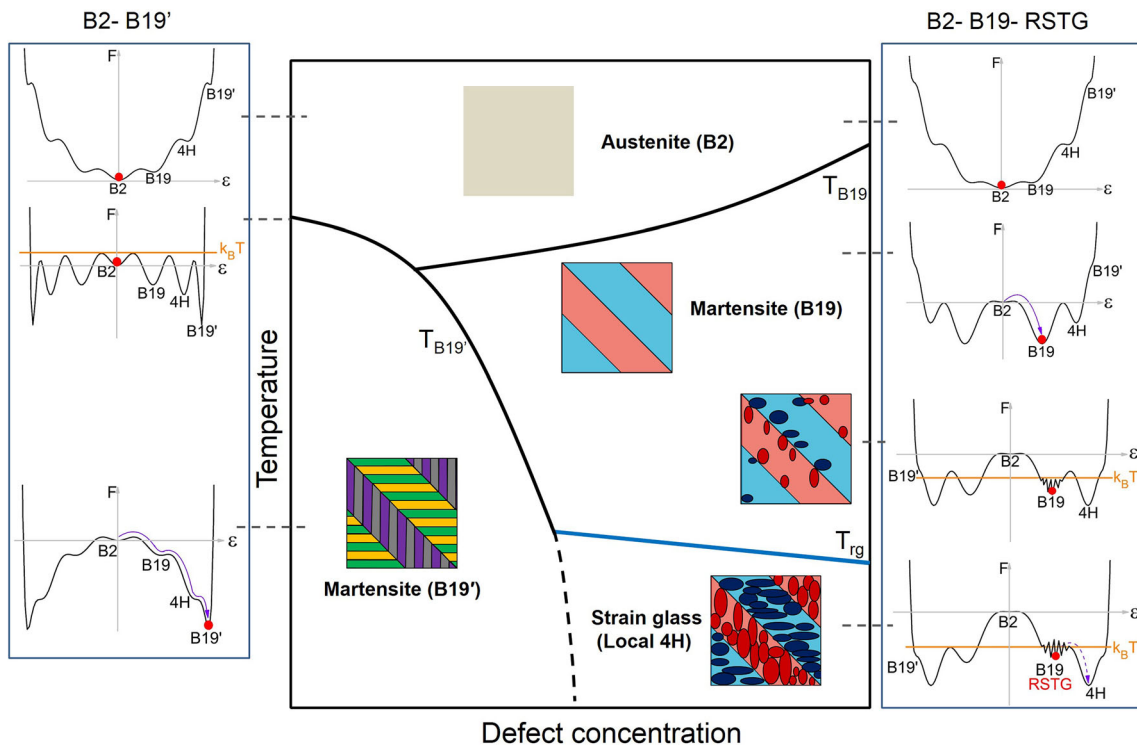

Fig. 6 Understanding of reentrant strain glass transition based on Landau free energy landscape. Without defect doping, system undergoes B2–B19' martensitic transformation directly. When defects doped, B2–B19–B19' two-step martensitic transition occurs. With more defects doped, system firstly undergoes B2–B19 transition and then reentrant stain glass transition: unfrozen 4H nanodomains appear within B19 martensitic matrix, upon cooling, those nanodomains become frozen, and more. Cu stabilizes B19 martensite instead of B19' martensite, thus once the system transits into B19 phase, with further cooling, due to the local energy barrier caused by point defects, the system is stacked at B19 phase and unable to transform into another martensitic phase of lower symmetry. As a result, only unfrozen nanodomains of 4H symmetry, lower than B19, emerge within B19 domains and finally become frozen and more numbered. [21] Reprinted from *Acta Materialia,* Vol 226, Wenjia Wang, Yuanchao Ji, Minxia Fang, Dong Wang, Shuai Ren, Kazuhiro Otsuka, Yunzhi Wang, Xiaobing Ren, Reentrant strain glass transition in Ti–Ni–Cu shape memory alloy, Page 117, 618, Copyright 2022, with permission from Elsevier

goes into the reentrant strain glass with local 4H symmetry, where the 4H phase is an intermediate phase between B19 phase and B19' phase.

It should be noted that $Ti_{50}Ni_{34}Cu_{16}$ cannot globally transform into the strain-ordered 4H phase due to the local barriers caused by Cu defects. Below T_{rg}, the kinetic energy $k_B T$ is still lower than the local barriers. Thus the 4H martensite is inaccessible because the system is trapped among the local barriers. Only nanodomains with local 4H symmetry appear within the B19 martensitic matrix.

Here, it should be noted that during the reentrant strain glass transition, the local symmetry breaking from B19 to 4H leads to the local symmetry-lowering or the increase of order of the system. Therefore, the RSTG state indeed has higher order than the B19 phase and thus the reentrant strain glass transition is thermodynamically possible [21].

Very recently, the reentrant strain glass transition has also been found in La-doped CaTiO3 (CaTiO3-100xLa) system. In the case of La-doped $CaTiO_3$, the random field caused by La dopants at $x > 0.65$ is not strong enough to suppress the 1st-step (C–T) ferroelastic/martensitic transition but strong enough to suppress 2nd-step (T–O) transition, thus a reentrant strain glass transition happens consequently [29].

Explanation of Previous Puzzles in Ti–Ni–Cu Shape Memory Alloys

Previously, it was known that in $Ti_{50}Ni_{50-x}Cu_x$ alloy system, when $x > 15$, only B2–B19 transition exists [25, 30]. However, many puzzling phenomena have been reported in $Ti_{50}Ni_{34}Cu_{16}$ alloy (Fig. 7): (i) below T_{B19}, additional small peaks that do not belong to the B19 structure exist in the synchrotron XRD results and (ii) the intensity of the additional peak increases when cooling from 230 to 90 K [31].

Now these puzzles can be explained by the reentrant strain glass transition. The additional small peaks in the synchrotron XRD results come from the 4H nanodomains, and the increasing intensity of the additional peak with cooling is due to the volume fraction increase of 4H nanodomains [21]. In short, the evolution of electron diffraction patterns in the in situ microstructural observations of reentrant strain glass transition is consistent with the evolution of the synchrotron XRD observations.

Spinodal Strain Glass

Strain glass is formed as a result of atomic/nanoscale randomness or random strain/stress field which disrupts the otherwise formation of long-range strain ordering or normal martensite [1–4]. So far, the atomic/nanoscale
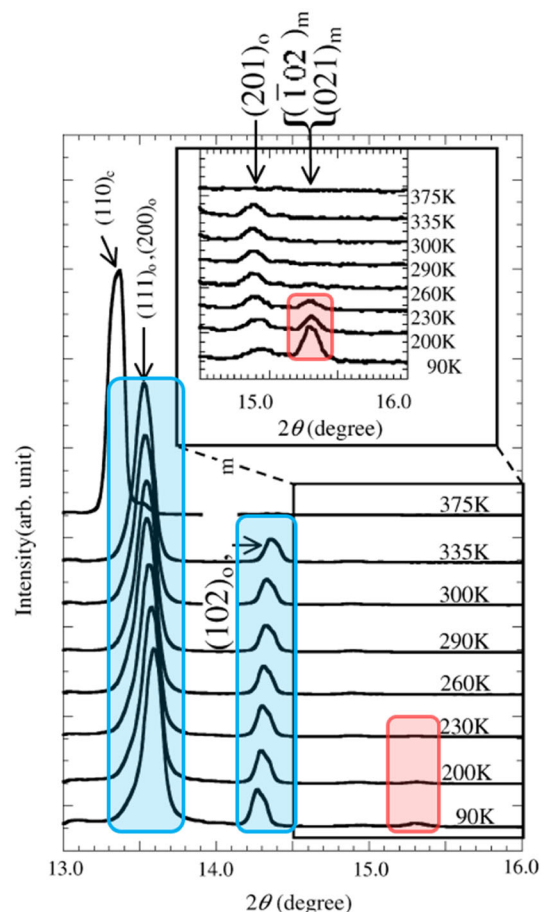

Fig. 7 In situ synchrotron X-ray diffraction observation results of $Ti_{50}Ni_{34}Cu_{16}$ alloy upon cooling with wavelength $\lambda = 0.049988$ nm. Besides the high peaks representing B19 orthorhombic phase, an additional small peak circled in red rectangle appear and the intensity of this peak increases with temperature decreasing from 230 to 90 K [31]. Reprinted from *Materials Science and Engineering: A,* Vol 438, T. Ohba, T. Taniwaki, H. Miyamoto, K. Otsuka, K. Kato, In situ observations of martensitic transformations in Ti50Ni34Cu16 alloy by synchrotron radiation, Pages 480–484, Copyright 2006, with permission from Elsevier

randomness can be created by point defects [1, 6], dislocations [19, 20], or nano-sized precipitates [7]. Contrasting with the above three conventional ways of achieving a strain glass, recently a non-conventional strain glass, i.e., spinodal strain glass, was reported [22]. It was achieved in a Mn–Cu alloy system which possesses both spinodal instability and martensitic instability [32, 33]: the spinodal decomposition can produce nanoscale compositional modulation that hinders the formation of normal martensite and as a result, a spinodal decomposition-induced strain glass is formed.

Contrast with the conventional strain glass which is formed from a homogeneous parent phase, the spinodal strain glass is formed from an unhomogeneous parent phase, i.e., the spinodally decomposed parent phase. In the
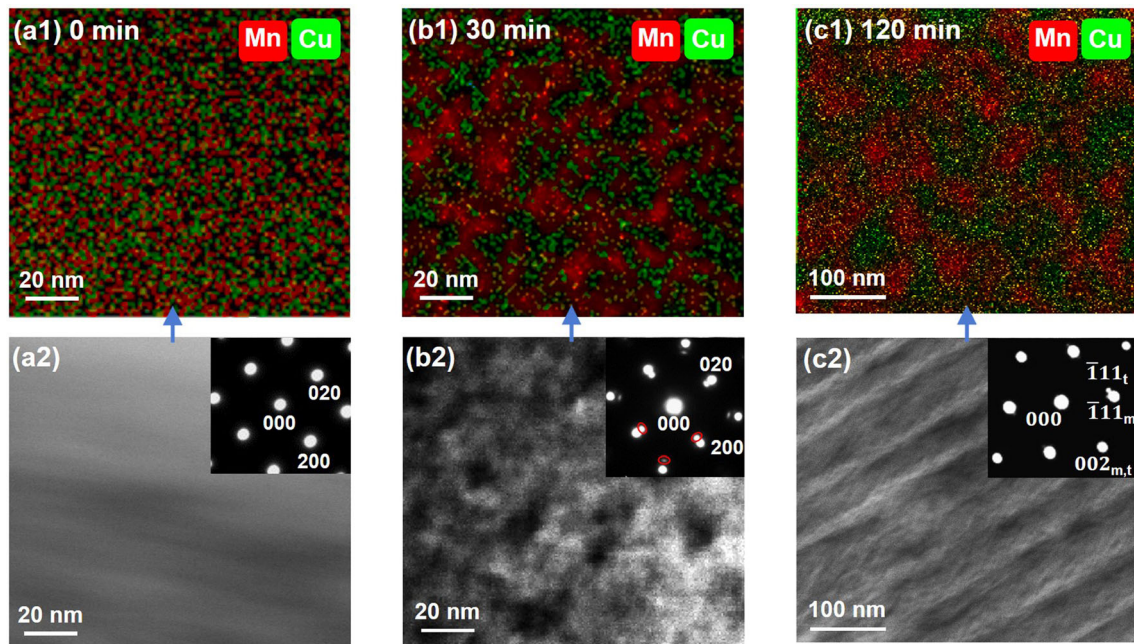
Fig. 8 STEM-EDS mapping of the $Mn_{60}Cu_{40}$ alloy aged for **a** 0 min, **b** 30 min, and **c** 120 min, respectively. (**a1**), (**b1**), and (**c1**) show the EDS mapping of Mn and Cu elements. (**a2**), (**b2**), and (**c2**) display the corresponding STEM image of (**a1**), (**b1**), and (**c1**), respectively [22].

following we shall show the evidence for spinodal decomposition and its effect on the formation of strain glass in Mn–Cu alloys.

Spinodal Decomposition in Aged $Mn_{60}Cu_{40}$ Alloys

Figure 8 shows the STEM-EDS composition mapping results of $Mn_{60}Cu_{40}$ alloy aged at 653 K for different times. In the as-quenched or 0-min-aged sample, the STEM-EDS composition mapping shows homogeneous Mn and Cu distributions (Fig. 8a), suggesting that the as-quenched state is compositionally homogeneous. The corresponding STEM image shows smooth morphology, suggesting the alloy is also structurally homogeneous, being face-centered-cubic (fcc) parent phase as evidenced by the inset diffraction pattern in Fig. 8a.

After aging at 653 K, a spinodal decomposition occurs in $Mn_{60}Cu_{40}$ and the size or wavelength of composition modulation changes greatly depending on aging time. Short-time aging (30 min), i.e., an early stage of spinodal decomposition produces nanoscale composition modulations with Mn-rich regions being 5–20 nm in size (Fig. 8b), and the corresponding STEM image shows a mottled or speckled morphology, which corresponds to face-centered tetragonal (fct) nanodomains as suggested by the inset additional fct diffraction spots. Long-time aging (120 min), i.e., a late stage of spinodal decomposition, produces

coarse composition modulations with Mn-rich regions being 40–80 nm in size as shown in Fig. 8c, and the corresponding STEM image shows large fct martensitic domains of $\sim$ 80 nm in width and > 400 nm in length.

Fct Martensitic Nanodomains in the Spinodal Strain Glass

Figure 9 shows the TEM and HREM results of $Mn_{60}Cu_{40}$ alloy aged for 30 min. The microstructure in Fig. 9a shows no martensitic twins, yet characterized by a mottled nanoscale morphology with fcc fundamental spots surrounded by diffuse satellite fct spots in the corresponding diffraction pattern (Fig. 9b). Dark-field image (Fig. 9c) obtained by selecting the circled fct satellite spot in Fig. 9b reveals randomly distributed fct nanodomains with $\sim$ 5 nm in size. This is the direct evidence for the existence of fct nanodomains of the spinodal strain glass in aged $Mn_{60}Cu_{40}$ alloy.

The HREM image in Fig. 9d reveals lattice image of the spinodal strain glass, of which the fast Fourier transform (FFT) spectrum shows the same feature with the taken diffraction pattern in Fig. 9b, i.e., existence of satellite fct spots. By selecting the satellite fct spots as arrowed in Fig. 9e, the inverse FFT image could be obtained (Fig. 9f), where many randomly distributed bright nano-regions (3–7 nm) exist. The FFT patterns of two selected areas in
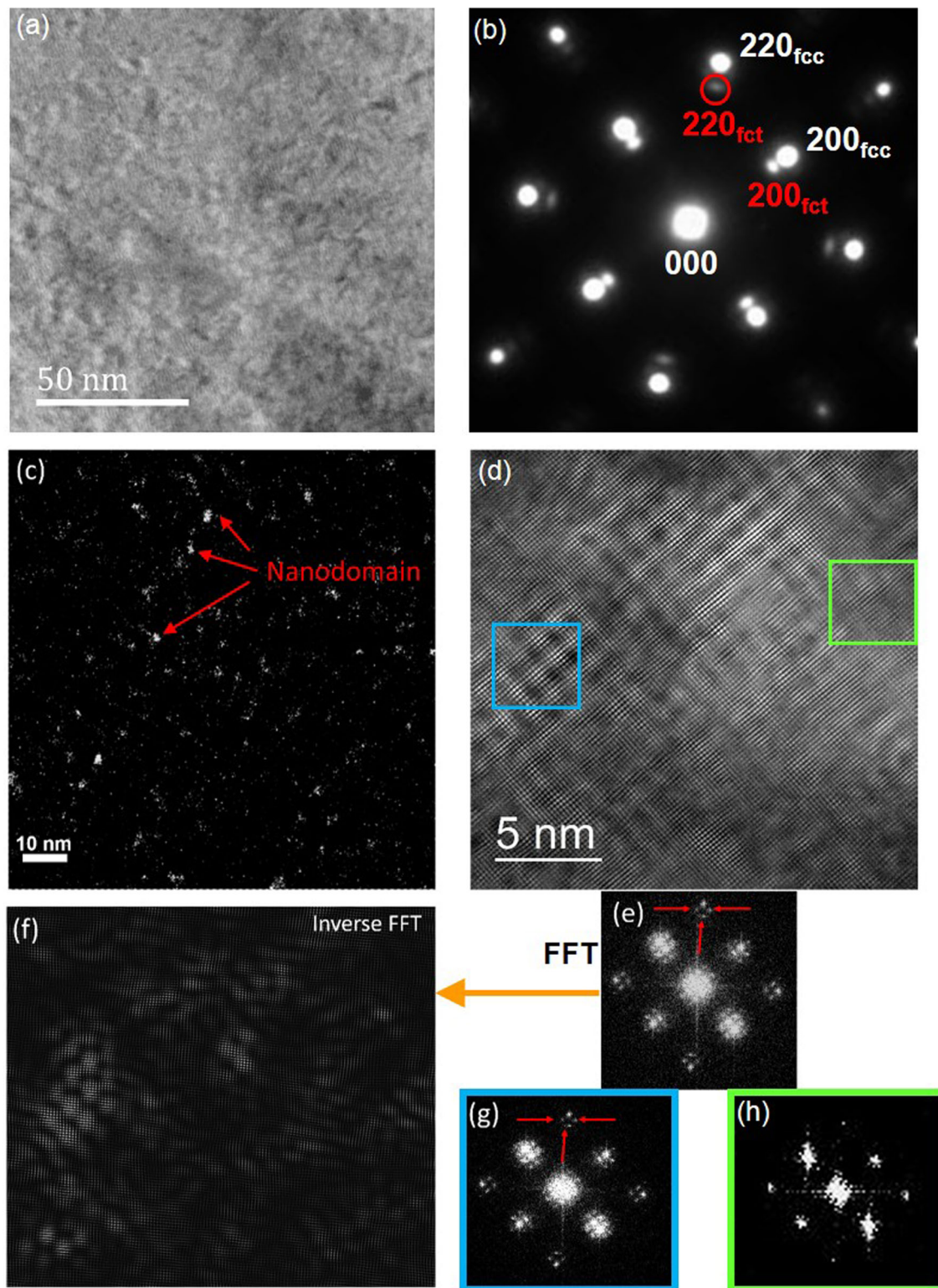
Fig. 9 TEM and HRTEM results of the $Mn_{60}Cu_{40}$ alloy aged for 30 min. **a** Bright-field image; **b** Diffraction pattern; **c** Dark-field image obtained by selecting the circled satellite spot in (**b**); **d** HRTEM image; **e** Fast Fourier transform (FFT) pattern of (**d**); **f** Inverse FFT image obtained by selecting the arrowed satellite spots in (**e**); **g** FFT pattern of the cyan square (nanodomain) in (**d**); **h** FFT pattern of the green square (matrix) in (**d**) [22]. Reprinted from *Acta Materialia*, Vol 231, Wenjia Wang, Pu Luo, Ying Wei, Yuanchao Ji, Chang Liu, Xiaobing Ren, Spinodal strain glass in Mn–Cu alloys, Page 117, 874, Copyright 2022, with permission from Elsevier

Fig. 10 Normalized electrical resistivity curves of the $Mn_{60}Cu_{40}$ alloys aged for different times [22]. Reprinted from *Acta Materialia,* Vol 231, Wenjia Wang, Pu Luo, Ying Wei, Yuanchao Ji, Chang Liu, Xiaobing Ren, Spinodal strain glass in Mn–Cu alloys, Page 117, 874, Copyright 2022, with permission from Elsevier
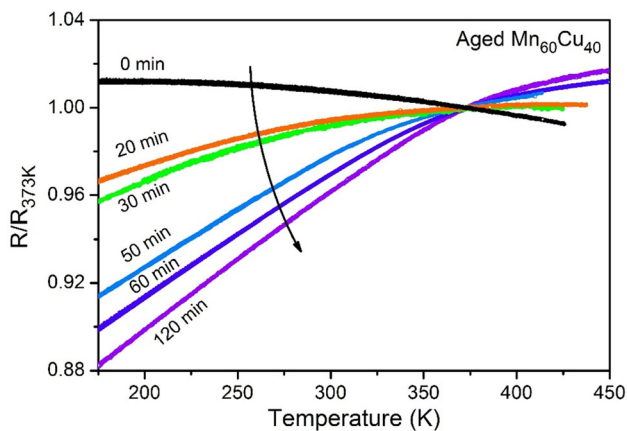
Fig. 9d further reveal that the cyan one has spot splitting and thus it corresponds to fct nanodomains; whereas the green one does not show spot splitting and thus corresponds to fcc matrix.

The formation of nanoscale fct domains in the spinodal strain glass sample can also be supported by electrical resistivity results, as shown in Fig. 10. The short-time-aged sample (i.e., strain glass sample) shows a decreasing resistivity with cooling, being same with the long-time-aged sample (i.e., martensitic sample), but the strain glass sample exhibits a weaker trend of resistivity decrease as compared with the martensitic sample. Considering the fct phase has lower specific resistivity than the fcc parent phase [32], a normal fcc–fct martensitic transformation will result in a significant decrease in resistivity, but a strain glass transition only results in a small decrease in resistivity.

Understanding of Spinodal Strain Glass Formation

The spinodal strain glass phase diagram of $Mn_{60}Cu_{40}$ as a function of aging time is shown in Fig. 11. There exists a critical aging time below which the strain glass transition occurs (i.e., spinodal strain glass) and above which a normal fcc–fct martensitic transformation occurs. For a long-time aged sample, spinodal decomposition is in its late stage and thus produces long-wavelength composition modulations with large Mn-rich and Mn-poor fcc regions. As a Mn-rich fcc region has strong driving force to transform into fct martensite, the fcc–fct martensitic transformation will start in the Mn-rich regions and then propagate through the surrounding Mn-lean regions and eventually forms a large martensite domain.
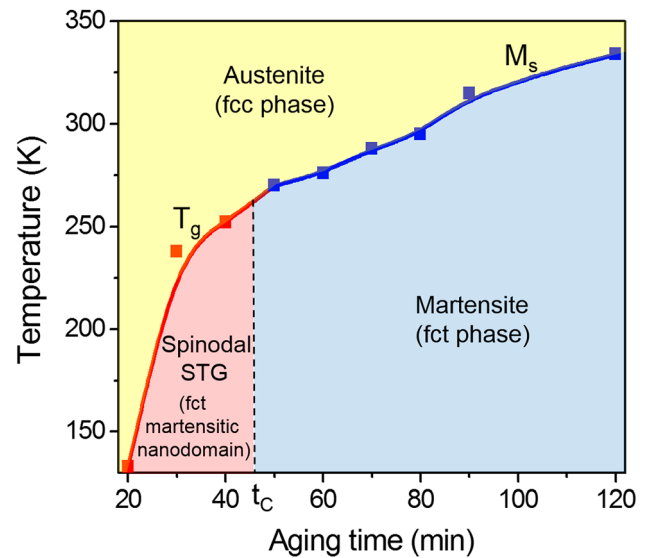

Fig. 11 Temperature vs. aging time phase diagram of spinodal strain glass of $Mn_{60}Cu_{40}$ alloys [22]. Reprinted from *Acta Materialia,* Vol 231, Wenjia Wang, Pu Luo, Ying Wei, Yuanchao Ji, Chang Liu, Xiaobing Ren, Spinodal strain glass in Mn–Cu alloys, Page 117, 874, Copyright 2022, with permission from Elsevier

However, by shortening aging time, spinodal decomposition is in its early stage and thus produces short-wavelength composition modulations with nano-sized Mn-rich and Mn-lean fcc regions, as shown in Fig. 8b. Although the Mn-rich fcc region tends to transform into fct martensite, a large scale or normal fcc–fct martensitic transformation cannot happen due to the nanoscale random field caused by the nanoscale composition modulations. As a result, a normal fcc–fct martensitic transformation is suppressed and instead a strain glass transition occurs.

Distinctiveness of Spinodal Strain Glass

The distinctiveness of spinodal strain glass is that besides the nanoscale structural inhomogeneity (i.e., existence of nano-sized martensitic domains) which is the fundamental feature of strain glass by definition, spinodal strain glass is derived from an inhomogeneous parent phase, i.e., spinodally decomposed parent phase, thus possessing the nanoscale compositional inhomogeneity (i.e., periodic composition modulations of Mn-rich and Mn-poor phases in nanoscale) [22]. As a result, the spinodal strain glass transition occurs over an even broader temperature range than conventional homogeneous strain glass alloys. Accordingly, some strain glass-related properties are expected for spinodal strain glass to persist over an ultra-wide temperature range, wider than conventional strain glass.

Figure 12 shows the comparison of Elinvar effect between Mn–Cu spinodal strain glass alloys (the 20-min-
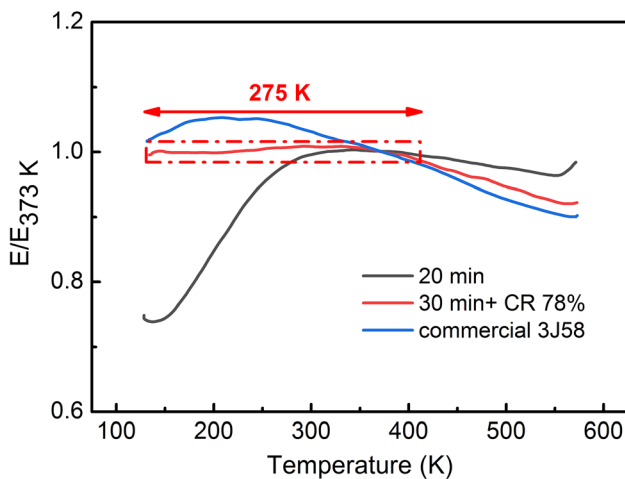
Fig. 12 Comparison of Elinvar effect between Mn–Cu spinodal strain glass alloys (the 20-min-aged sample, and the 30-min-aged sample followed by 78% cold rolling) with the commercial magnetic Elinvar alloy 3J58 [22]. Reprinted from *Acta Materialia,* Vol 231, Wenjia Wang, Pu Luo, Ying Wei, Yuanchao Ji, Chang Liu, Xiaobing Ren, Spinodal strain glass in Mn–Cu alloys, Page 117, 874, Copyright 2022, with permission from Elsevier

Fig. 13 Comparison of the temperature range of Elinvar effect vs. the damping property (tan δ) within this temperature range of different Elinvar alloys. Inset shows tan δ as a function of temperature of 20-min-aged spinodal strain glass alloy, cold-rolled 30-min-aged spinodal strain glass alloy, and commercial Elinvar alloy 3J58 [22]. Reprinted from *Acta Materialia,* Vol 231, Wenjia Wang, Pu Luo, Ying Wei, Yuanchao Ji, Chang Liu, Xiaobing Ren, Spinodal strain glass in Mn–Cu alloys, Page 117, 874, Copyright 2022, with permission from Elsevier

aged sample, and the 30-min-aged sample followed by 78% cold rolling) with the commercial magnetic Elinvar alloy 3J58. The modulus for cold-rolled 30-min-aged sample keeps invariant over a superwide temperature range of 275 K (from 133 to 408 K), superior to the commercial ferromagnetic Elinvar alloy 3J58. Furthermore, the spinodal strain glass also possesses high damping property over a wide temperature range. Such a remarkable property is not possessed by other non-magnetic or magnetic Elinvar alloys. As shown in Fig. 13, the spinodal strain glass MnCu alloys possess the highest damping property, with tan δ as high as 0.045, in sharp contrast with other main Elinvar alloys, which show very low damping [22]. In short, the spinodal strain glass alloy is a high-damping, non-magnetic Elinvar alloy within a very wide temperature window of 275 K.

Summary and Outlook

In this article, we have reviewed recent progress in two types of non-conventional strain glasses (i.e., reentrant strain glass and spinodal strain glass) and their novel properties. Reentrant strain glass is a strain glass formed from a martensite matrix, contrasting with the conventional strain glass where strain glass is formed from a parent phase matrix. It exhibits interesting properties such as low-modulus Elinvar effect and high damping over a broad temperature range. Our recent work further shows that an unusual low-temperature toughening phenomenon down to cryogenic temperature (a significant increase in both
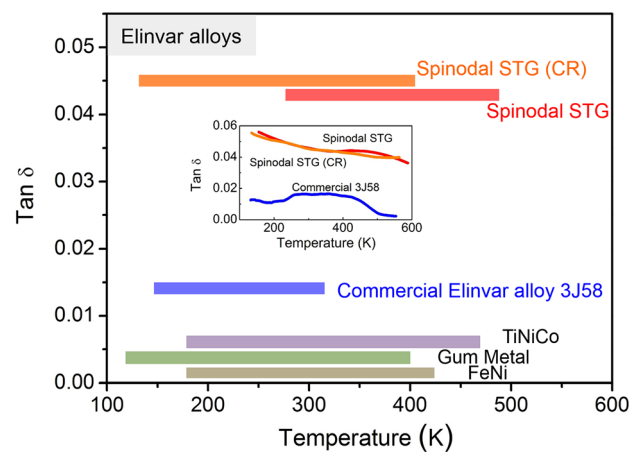
fracture toughness and strength from 323 to 123 K) is found in the reentrant strain glass of brittle systems, like ceramics, which may provide a way to design tough materials with wide working temperature range. Spinodal strain glass is a strain glass formed from spinodally decomposed parent phase with nanoscale compositional inhomogeneity. It shows Elinvar effect and high damping over a very wide temperature range. Therefore, these non-conventional strain glass alloys may open a new horizon for novel structural/functional materials.

References

1. Sarkar S, Ren X, Otsuka K (2005) Evidence for strain glass in the ferroelastic-martensitic system Ti$_{50-x}$Ni$_{50+x}$. Phys Rev Lett 95:205702
2. Ji Y, Ren S, Wang D, Wang Y, Ren X (2018) Strain glasses. In: Lookman T, Ren X (eds) Frustrated materials and ferroic glasses. Springer, Berlin, pp 183–204
3. Ji Y, Wang D, Wang Y, Zhou Y, Xue D, Otsuka K, Wang Y, Ren X (2017) Ferroic glasses. npj Comput Mater 3:43
4. Ren X (2014) Strain glass and ferroic glass-unusual properties from glassy nano-domains. Phys Status Solidi B 251:1982–1992
5. Liu C, Ji Y, Tang J, Otsuka K, Wang Y, Hou M, Hao Y, Ren S, Luo P, Ma T, Wang D, Ren X (2022) A lightweight strain glass

alloy showing nearly temperature-independent low modulus and high strength. Nat Mater 21:1003–1007

6. Zhou Y, Xue D, Ding X, Wang Y, Zhang J, Zhang Z, Wang D, Otsuka K, Sun J, Ren X (2010) Strain glass in doped $Ti_{50}(Ni_{50-x}D_x)$ (D = Co, Cr, Mn) alloys: implication for the generality of strain glass in defect-containing ferroelastic systems. Acta Mater 58:5433–5442

7. Ji Y, Ding X, Lookman T, Otsuka K, Ren X (2013) Hetero-geneities and strain glass behavior: role of nanoscale precipitates in low-temperature-aged $Ti_{48.7}Ni_{51.3}$ alloys. Phys Rev B 87:104110

8. Chien C, Tsao CS, Wu SK, Chang CY, Chang PC, Kuo YK (2016) Characteristics of the strain glass transition in as-quenched and 250 °C early-aged $Ti_{48.7}Ni_{51.3}$ shape memory alloy. Acta Mater 120:159–167

9. Ji Y, Wang D, Ding X, Otsuka K, Ren X (2015) Origin of an isothermal R-martensite formation in Ni-rich Ti–Ni solid solution: crystallization of strain glass. Phys Rev Lett 114:055701

10. Sun X, Cong D, Ren Y, Liss K-D, Brown DE, Ma Z, Hao S, Xia W, Chen Z, Ma L, Zhao X, He Z, Liu J, Li R, Wang Y (2020) Magnetic-field-induced strain-glass-to-martensite transition in a Fe–Mn–Ga alloy. Acta Mater 183:11–23

11. Liang C, Wang D, Wang Z, Ding X, Wang Y (2020) Revealing the atomistic mechanisms of strain glass transition in ferroelastics. Acta Mater 194:134–143

12. Ji Y, Zhang P, He L, Wang D, Luo H, Otsuka K, Wang Y, Ren X (2019) Tilt strain glass in Sr and Nb co-doped $LaAlO_3$ ceramics. Acta Mater 168:250–260

13. Yao Y, Yang Y, Ren S, Zhou C, Li L, Ren X (2012) Ferroelastic and strain glass transition in $(1–x)(Bi_{0.5}Na_{0.5})TiO_3$-$xBaTiO_3$ solid solution. Europhys Lett 100:17004

14. Liang Q, Wang D, Zheng Y, Zhao S, Gao Y, Hao Y, Yang R, Banerjee D, Fraser HL, Wang Y (2020) Shuffle-nanodomain regulated strain glass transition in Ti-24Nb-4Zr-8Sn alloy. Acta Mater 186:415–424

15. Zhou Y, Xue D, Tian Y, Ding X, Guo S, Otsuka K, Sun J, Ren X (2014) Evidence for local symmetry breaking during a strain glass transition. Phys Rev Lett 112:025701

16. Wang D, Hou S, Wang Y, Ding X, Ren S, Ren X, Wang Y (2014) Superelasticity of slim hysteresis over a wide temperature range by nanodomains of martensite. Acta Mater 66:349–359

17. Ren S, Xue D, Ji Y, Liu X, Yang S, Ren X (2017) Low-field-triggered large magnetostriction in iron-palladium strain glass alloys. Phys Rev Lett 119:125701

18. Wang D, Wang Y, Zhang Z, Ren X (2010) Modeling abnormal strain states in ferroelastic systems: the role of point defects. Phys Rev Lett 105:205702

19. Zhang J, Xue D, Cai X, Ding X, Ren X, Sun J (2016) Dislocation induced strain glass in $Ti_{50}Ni_{45}Fe_5$ alloy. Acta Mater 120:130–137

20. Liang Q, Wang D, Zhang J, Ji Y, Ding X, Wang Y, Ren X, Wang Y (2017) Novel B19' strain glass with large recoverable strain. Phys Rev Mater 1:033608

21. Wang W, Ji Y, Fang M, Wang D, Ren S, Otsuka K, Wang Y, Ren X (2022) Reentrant strain glass transition in Ti-Ni-Cu shape memory alloy. Acta Mater 226:117618

22. Wang W, Luo P, Wei Y, Ji Y, Liu C, Ren X (2022) Spinodal strain glass in Mn-Cu alloys. Acta Mater 231:117874

23. Alguero M, Gregg JM, Mitoseriu L (2016) Nanoscale ferro-electrics and multiferroics: key processing and characterization issues, and nanoscale effects. Wiley, West Sussex, UK

24. Mydosh JA (1993) Spin glasses: an experimental introduction. Taylor & Francis, London

25. Otsuka K, Ren X (2005) Physical metallurgy of Ti-Ni-based shape memory alloys. Prog Mater Sci 50:511–678

26. Potapov P, Shelyakov A, Schryvers D (2001) On the crystal structure of TiNi-Cu martensite. Scr Mater 44(1):1–7

27. Nishiyama Z (1978) Martensitic transformation. Academic Press, Cambridge

28. Zhang Z, Wang Y, Wang D, Zhou Y, Otsuka K, Ren X (2010) Phase diagram of $Ti_{50-x}Ni_{50+x}$: crossover from martensite to strain glass. Phys Rev B 81:224102

29. Fang M, Ji Y, Ni Y, Wang W, Zhang H, Wang X, Xiao A, Ma T, Yang S, Ren X (2023) Toughen ceramics down to cryogenic temperatures by reentrant strain glass transition. Phys Rev Lett 130:116102

30. Nam TH, Saburi T, Shimizu K (1990) Cu-content dependence of shape memory characteristcs in Ti-Ni-Cu alloys. Mater Trans JIM 31(11):959–967

31. Ohba T, Taniwaki T, Miyamoto H, Otsuka K, Kato K (2006) In situ observations of martensitic transformations in $Ti_{50}Ni_{34-}Cu_{16}$ alloy by synchrotron radiation. Mater Sci Eng A 438:480–484

32. Tsuchiya K, Sato H, Edo S, Marukawa K, Umemoto M (1999) Correlation between fcc–fct transformation behavior and spinodal decomposition in γ-MnCu alloys. Mater Sci Eng A 273:181–185

33. Yang J, Zhao C, Liang H, Wang Z, Su C (2021) Spinodal decomposition and martensitic transformation of the high manganese Mn–x Cu alloys fabricated by additive manufacturing. Appl Mater Today 25:101170